Multilayer Diffraction Reveals That Colloidal Superlattices Approach the Structural Perfection of Single Crystals

Stefano Toso[1,2,†], Dmitry Baranov[1,†,*], Davide Altamura[3], Francesco Scattarella[3], Jakob Dahl[4,5], Xingzhi Wang[4,5], Sergio Marras[6], A. Paul Alivisatos[4,5,7,8], Andrej Singer[9], Cinzia Giannini[3,*], Liberato Manna[1,*]

[1]Nanochemistry Department, Istituto Italiano di Tecnologia, Via Morego 30, 16163, Italy

[2]International Doctoral Program in Science, Università Cattolica del Sacro Cuore, 25121 Brescia, Italy

[3]Istituto di Cristallografia - Consiglio Nazionale delle Ricerche (IC-CNR), Via Amendola 122/O, I-70126 Bari, Italy

[4]Department of Chemistry, University of California Berkeley, Berkeley, California 94720, USA

[5]Materials Sciences Division, Lawrence Berkeley National Laboratory, California 94720, USA

[6]Materials Characterization Facility, Istituto Italiano di Tecnologia, Via Morego 30, 16163, Italy

[7]Department of Materials Science and Engineering, University of California Berkeley, Berkeley, California 94720, USA

[8]Kavli Energy NanoScience Institute, Berkeley, California 94720, USA

[9]Department of Materials Science and Engineering, Cornell University, Ithaca, New York 14850, United States

[†]S.T. and D.B. contributed equally.

*Corresponding authors: dmitry.baranov@iit.it, cinzia.giannini@ic.cnr.it, liberato.manna@iit.it

Contents:

S.a Low-angle region

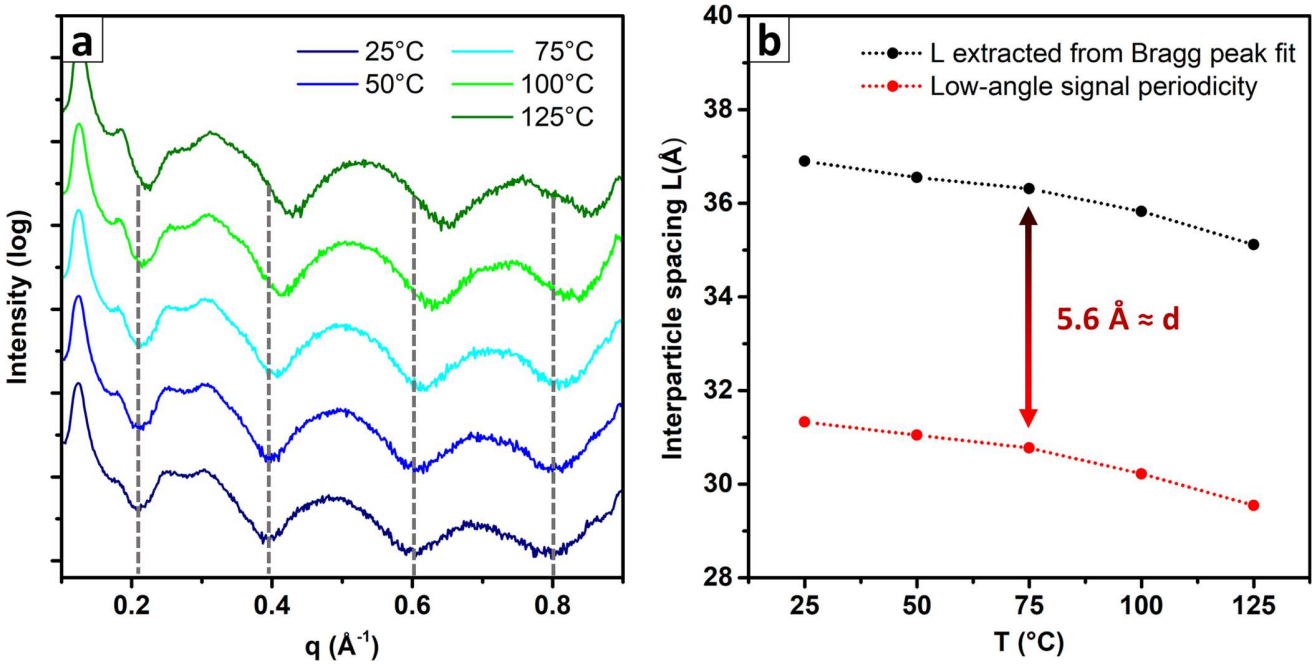

Figure S1. Temperature dependence of the low-angle signal and extracted interparticle spacing. a) The periodically modulated signal at low angles evolves with temperature during the annealing experiment. The X-ray scattering intensity is plotted on a logarithmic scale and data recorded at different temperatures are offset for clarity. Vertical dashed lines mark the position of the dips at the start of the experiment at 25°C. b) The comparison between interparticle spacing *L* extracted from the low-angle data (red solid circles) and from the multilayer diffraction model fit of the first Bragg peak (black solid circles). The two differ by a nearly constant value of 5.56 ± 0.04 Å.

The low-angle region of $CsPbBr_3$ nanocrystal superlattices patterns contained broad periodically modulated signals which gradually shifted under thermal annealing (Figure S1a). At room temperature, the modulation periodicity measured at the signal minima was 0.201 $Å^{-1}$, corresponding to a period of 31.3 Å in the real space. Upon heating, the signal minima shifted towards higher angles and the periodic inter-minima distance broadened, corresponding to the shortening of the period in real space to 29.5 Å at 125°C. That trend parallels the contraction of the interparticle spacing *L* extracted by the multilayer diffraction model (L=36.9→35.1 Å), while the absolute values differ by 5.56 ± 0.04 Å (Figure S1b). The ≈5.6 Å mismatch is explained by the nature of the low-angle scattering data. At low angles, X-ray scattering is sensitive to the nanometer-scale electron density modulation, as depicted in Figures 1d and S2a. The low-angle diffraction pattern represents a Fourier transform power spectrum of the electron density modulation in the sample. The superlattice electron density in the direction normal to the substrate can be represented by a "pulse train" profile (Figure S2a) where regions of high electron density correspond to inorganic nanocrystals and regions of low electron density correspond to organic ligands between them. The scattered intensity can be approximated by a $sinc^2$ function:

$$I(q) = \left(\frac{\sin(width \cdot q)}{(width \cdot q)}\right)^2 \qquad \text{Eq. S1}$$

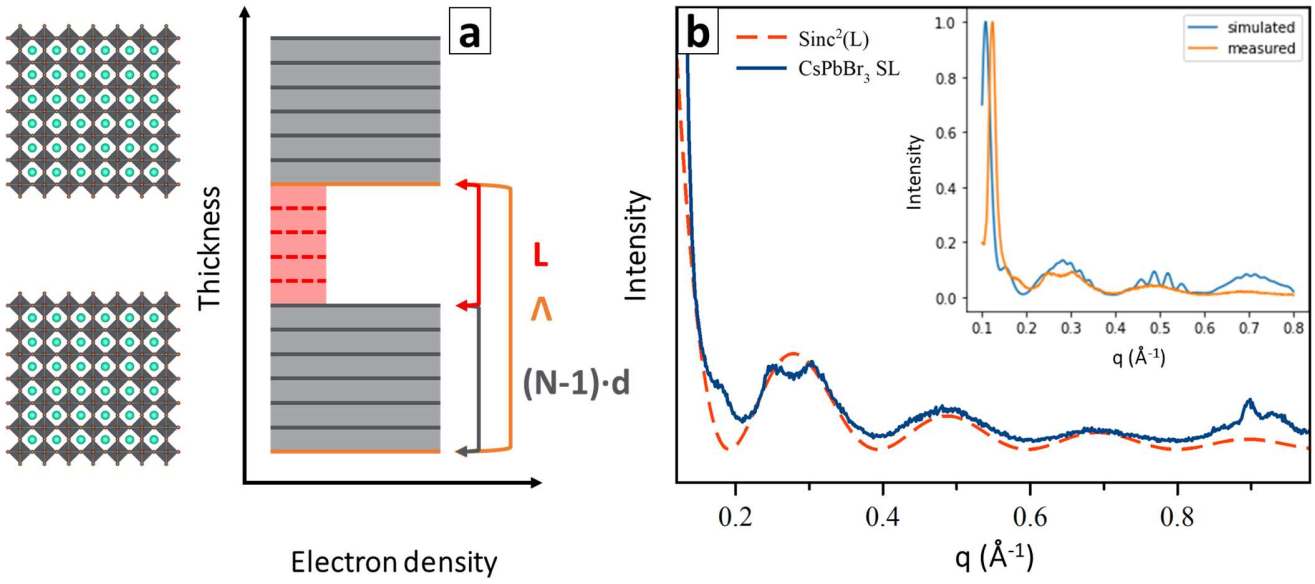

Figure S2. Origin of the low-angle periodic signals. a) The nanometer-scale electron density modulation in the superlattice is represented as a pulse train, of which the diffraction experiment performs the Fourier transform. b) The low-angle signal can be described as a power spectrum of the low amplitude part of the pulse train, namely the interparticle spacing, and approximated by a sinc^2 function. The inset shows how the multilayer diffraction model reproduces the low-angle region of the pattern.

The width found in Equation S1 is that of the considered section of the pulse train. For the low electron density part, which is the one reproducing the low-angle profile, the width is described as $d{\cdot}M$, where $M = L/d - 1$ represents the number of virtual crystal planes found within the interparticle spacing and represented by the red dashed lines in Figure S2a. The -1 comes from the extremes of the interparticle spacing, that belong to the nanocrystals and should not be counted twice, providing an explanation for the ≈5.6 Å periodicity mismatch (Figure S1b).The resulting profile approximates both the periodicity and the intensity of the broad periodical signal found at low-angles (Figure S2b).

The multilayer diffraction model qualitatively accounts for all the low-angle signal features (superlattice Bragg peak and broad periodical signals, inset of Figure S2b). However, we decided not to include it in the fit: the natural broadening of signals at low angles smears out most of its fine structure, and the measured intensity is strongly dependent on the incidence angle (thus requiring additional corrections in the model). In addition, the analysis of extremely low-angle data (*i.e.* q<0.2 Å^{-1}) is strongly influenced by residual misalignments and deviations due to the non-negligible refraction of X-rays and dynamical scattering phenomena. Taking into account these effects would complicate the model beyond its intended purpose.

S.b Multilayer Diffraction model and its implementation

General model structure

The Multilayer Diffraction model we used to fit the θ:2θ XRD patterns is based on the work of Fullerton *et. al.*[1] The original algorithm was developed for epitaxially grown binary multilayers, thus it describes the sample as a periodic stack of bilayers. We kept the bilayer description, even if redundant for a single-material superlattice, in order to ease the model implementation. Simply, the two materials in the bilayer are identical. Our algorithm takes a 2D-array of scattered intensity (counts) *vs* scattering vector (q, $Å^{-1}$) as an input. 2θ→q conversion, background subtraction and intensity corrections must be performed beforehand (see Methods). In total, the algorithm considers five parameters related to the superlattice structure, one instrumental parameter, and three constants (Table S1).

Table S1. Parameters of the Multilayer Diffraction model. This table summarizes the structural (blue) and instrumental (green) parameters considered by the Multilayer Diffraction model, explaining their conceptual role and their effect on the simulated profile.

Parameter	Role	Effect on the diffraction profile
d **(Å)**	Is the periodicity of the atomic planes generating the Bragg peaks.	Centers the interference convolution profile in the q-scale, takes part in the determination of *L* together with *N* and *d*. Sensitive to *q-zero correction*.
L **(Å)**	Is the interparticle spacing, defined as the distance between the two closest atomic planes of neighboring nanocrystals.	Centers the position of fringes. Depends on *d*, *L* and *N*. It is characterized by a series of relative minima in the χ^2/L plot, which can complicate its determination.
σ_L **(Å)**	Represents the stacking disorder of nanocrystals in terms of statistical fluctuation of the local interparticle spacing.	Smears the superlattice fringes. It is crucial for observing the superlattice interference: if disorder is too high fringes disappear, and only a peak profile dependent on *d* and *N* remains visible.
N **(at. planes)**	Represents the nanocrystals thickness expressed in numbers of atomic planes.	Determines the broadening of the interference convolution profile. Together with *d* it defines the nanocrystal form factor.
σ_N **(at. planes)**	Represents the size distribution broadening of nanocrystals in the sample.	It has a small effect on the simulated pattern. Mainly, it smears the outermost, low-intensity fringes of the convolution.
q-zero correction **($Å^{-1}$)**	Compensates for small misalignments of the diffractometer. Must be small, on the order of ± 0 - 0.02 $Å^{-1}$.	Shifts the q-scale by a constant. Shifts the periodic signals in the pattern (*i.e.* superlattice fringes and Bragg peaks) so that they are found at q-vales multiple of each other. Affects determination of *d* and *L*, which are related by the equation $\Lambda = d \cdot (N-1) + L$.
Instrumental broadening **($Å^{-1}$)**	Considers the broadening of signals in the diffractogram due to the instrumental contribution. This parameter must be determined experimentally.	A Gaussian of constant σ is convoluted on the top of the computed pattern before comparing it to the experimental data. Causes the broadening of all the diffraction features.
Coherence length **(n. of nanocrystals)**	Is the number of nanocrystals which are illuminated by coherent radiation.	Should be set high enough to have no effect on the diffraction pattern, because the structural coherence dominates. We set it to a constant value of 20 nanocrystals.
Experimental intensity fluctuation **(%)**	It is used by the bootstrap algorithm to evaluate the error bars on fitted parameters. Must be determined experimentally.	No effect on the fit.

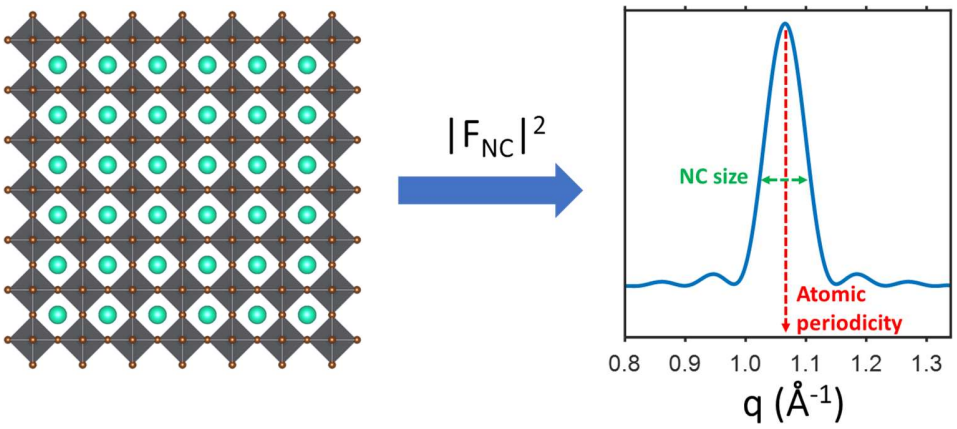

Figure S3. Nanocrystal form factor. An individual nanocrystal generates a diffraction profile which depends solely on the atomic lattice periodicity *d* and on the nanocrystal size *N*. This profile is the envelope that convolutes the intensity of the superlattice fringes.

Implementation

The Multilayer Diffraction model calculates the diffraction profile of an ensemble of superlattices. Each superlattice is size-pure (*i.e.* contains only nanocrystals of one specific size). The model sums the contribution of many superlattices formed by particles of different sizes to account for the nanocrystal size distribution. As a very first step, the model computes a Gaussian distribution of nanocrystal sizes, based on *N* and σ_N. This will be used to weight the contributions of each size to the overall diffraction profile.

$$P_N = \frac{1}{\sigma_N \sqrt{2\pi}} e^{-\frac{1}{2}\left(\frac{N_0 - N}{\sigma_N}\right)^2} \qquad \text{Eq. S2}$$

Note about P_N: The P_N distribution is discrete, *i.e.* only integer values of *N*, *i.e.* unit cells in a nanocrystal, are considered, because each atomic layer represents a scattering center. Any fractional description would be meaningless. For calculation purposes, the distribution is truncated at $N \pm 3\,\sigma_N$.

For each nanocrystal size in the distribution, the model performs the following routine. First step, the algorithm computes the single nanocrystal form factor:

$$F(q) = \frac{1 - e^{i \cdot N d \cdot q}}{1 - e^{i \cdot d \cdot q}} \qquad \text{Eq. S3}$$

Second step, using $F(q)$ and *N* the algorithm computes additional factors needed to describe the diffracted intensity:

$$|F|^2 = F(q) \cdot F(q)^* \qquad \text{Eq. S4}$$

$$T(q) = e^{i \cdot (N-1) d \cdot q} \qquad \text{Eq. S5}$$

$$\Phi(q) = T \cdot F(q)^* \qquad \text{Eq. S6}$$

Where $|F|^2$ is the intensity profile diffracted by a single nanocrystal, as shown in Figures 2a and S3. $T(q)$ is a factor responsible for the phase mismatch due to the spacing between adjacent nanocrystals, and the $\Phi(q)$is pre-calculated just to shorten Equation 9, where the product it represents recourses frequently.

Note about F(q): In the work of Fullerton et. al[1], the model computes the average $\langle F(q) \rangle$ for all the possible layer thicknesses instead of the size-pure F(*q*) factor as we did. In our case, we simply describe the total diffracted intensity I(*q*) as sum of all the possible I(q, N)'s weighted according to the P_N distribution. This is a valid assumption as the X-ray experiment measures an ensemble, not a single superlattice.

Third step, the model computes a distribution for the interparticle spacing values, which is a Gaussian centered in *L* with a standard deviation of σ_L.

$$P_L = \frac{1}{\sigma_L \sqrt{2\pi}} e^{-\frac{1}{2}\left(\frac{L-L}{\sigma_L}\right)^2} \qquad \text{Eq. S7}$$

Unlike the others, Equation S7 does not appear explicitly in the model by Fullerton et *al*. Instead, they considered its effects by introducing the distribution-dependent factor *ξ*, which is the one effectively computed by the algorithm. The mathematical description is equivalent: for the demonstration please refer to the original publication.[1]

$$\xi = i \cdot qL - \frac{q^2 \sigma_L^2}{2} \qquad \text{Eq. S8}$$

Fourth step, the coherence length *C* (number of nanocrystals which diffract coherently, see section S.f), $|F|^2$, Φ, T, and ξ are combined to calculate the diffracted intensity I(*q,N*) as follows (see Ref.1 for the in-depth discussion and derivation of Equation S9):

$$I(q, N) = 2C \cdot \left[|F|^2 + \mathrm{Re}\left(e^{\xi} \Phi F\right)\right] + 2\,\mathrm{Re}\left[\Phi F \left(\frac{e^{-\xi}}{T^2} + \frac{2}{T} + e^{\xi}\right) \times \left(\frac{C - (C+1)e^{2\xi}T^2 + \left(e^{2\xi}T^2\right)^{C+1}}{\left(1 - e^{2\xi}T^2\right)^2} - C\right)\right] \qquad \text{Eq. S9}$$

Fifth step, the total diffracted intensity of the sample is computed by adding up the I(*q,N*) contributions according to the P_N probability distribution:

$$I(q)_{tot} = \sum_{i=N-3\sigma N}^{N+3\sigma N} P_i \cdot I(q, i) \qquad \text{Eq. S10}$$

Sixth step, the calculated $I(q)_{tot}$ is convoluted with the instrumental peak profile. The instrumental peak profile is represented as a Gaussian with a broadening σ_G. We estimated it experimentally from the Gaussian fit of a LaB_6 standard diffraction pattern (peak at q = 1.51 Å^{-1}, σ = 0.007 Å^{-1}):

$$I(q)_{calc} = \int_q I(q)_{tot} \cdot e^{-\frac{1}{2}\left(\frac{q-\tau}{\sigma_G}\right)^2} d\tau \qquad \text{Eq. S11}$$

Seventh and the last step, the computed $I(q)_{calc}$ is intensity-normalized to match the peak of the experimentally measured I(*q*) and compared with the experimental data. The best fit parameters are found by minimizing the sum of least squares:

$$x^2 = \sum_q (I(q)_{calc} - I(q)_{obs})^2 \qquad \text{Eq. S12}$$

The fitting procedure was automated by using the scipy.optimize.least_squares routine to minimize the sum of least squares, given the starting value and upper and lower boundaries for each parameter in the model. The reader is referred to the code provided in Supporting Information for an example.

We point out that the superlattice periodicity Λ is a derived parameter due to implementation reasons. It is convenient to calculate Λ by using the value of most probable nanocrystal size N rounded to the closest integer minus one (to avoid double-counting of the outermost atomic planes which is included in L, see Figure 2 in the main text), d, and L (see Table S1 for definitions):

$$\Lambda \pm \sigma_{\Lambda} = [(N_{int} - 1) \cdot d + L] \pm \sqrt{[(N-1) \cdot \varepsilon_d]^2 + \varepsilon_L^2} \qquad \text{Eq. S13}$$

Where σ_{Λ} is calculated according to error propagation formulas, while ε_d and ε_L represent the uncertainty associated with the parameters d and L respectively as estimated by bootstrap (section S.j).

S.c Physical meaning of L

In our fitting model, the *L* parameter represents the distance between two adjacent crystalline cores. This distance comprises the outermost nanocrystal atoms and the organic ligands passivating its surface (Figure S4). We assume that the surface chemistry of nanocrystals is independent from the nanocrystal size, thus the interparticle spacing can be considered constant for all the superlattices. However, due to the "soft" nature of the ligands, *L* can be locally thickened or thinned, causing a random nanocrystal misplacement. Such continuous disorder is captured by the parameter σ_L, whose main effect on the pattern is to let the interference fringes appear or fade according to the degree of the disorder (Figure 3c). Right after the self-assembly, the organic layer between nanocrystals also contains trapped residual solvent molecules (or in general any volatile molecule coming from the synthesis), which are removed from the superlattices under vacuum.[2]

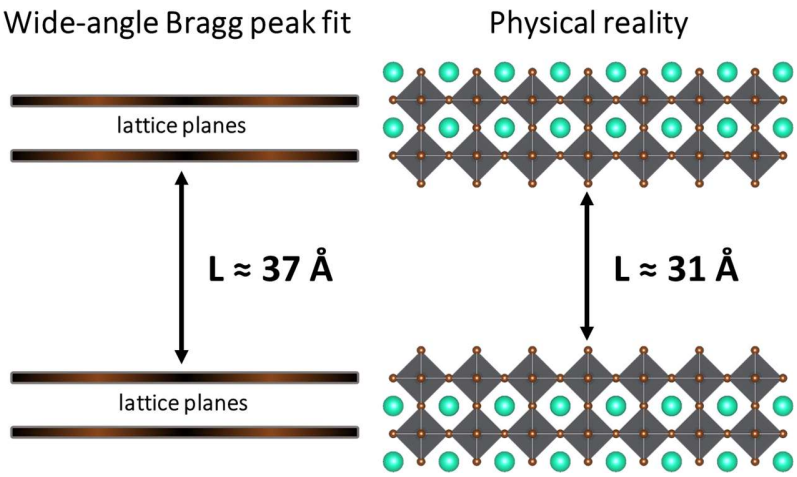

Figure S4. Thickness of $CsPbBr_3$ nanocrystals. The Multilayer Diffraction model measures the nanocrystal thickness in terms of Pb-Br_2 planes. However, the $CsPbBr_3$ nanocrystals are oleylammonium bromide-terminated, thus the real thickness increases by *d*, while the interparticle spacing decreases by the same amount with respect to the fitted parameter.

S.d Physical meaning of N and nanocrystal thickness

The Multilayer Diffraction model measures the thickness of nanocrystals in terms of atomic planes *N*. As a consequence, the crystal structure and the surface termination layer of the inorganic core must be considered when converting *N* into a thickness in nanometers. Taking the case of PbS nanocrystals, particles are formed by layers of Pb-S that are all identical to each other. The Multilayer Diffraction method measures $N = 4$ planes with a periodicity $d = 3.02$ Å, and the thickness is simply given by $(N-1)\cdot d = 9.07$ Å.

The case of $CsPbBr_3$ nanocrystals is different. The first Bragg peak corresponds to the pseudocubic (100) planes, which have a periodicity of $d = 5.84$ Å, compatible with both the Cs-Br planes and the Pb-Br_2 planes in the structure. However, the Pb-Br_2 planes are the most electron dense (152 e^-/unit cell in $PbBr_2$ *vs* 90 e^-/unit cell in CsBr planes, calculated by summing up the total number of electrons per formula unit), thus we consider them as the main scattering entities. The Multilayer Diffraction method measures $N = 13$, meaning that nanocrystal are 13 Pb-Br_2 planes thick. However, $CsPbBr_3$ is oleylammonium bromide-terminated, thus an extra Pb-Br bond should be considered on each side (≈ 2.92×2 = 5.84 Å, Figure S3), raising the nanocrystal thickness to $N\cdot d \approx 76$ Å. As a consequence, the actual interparticle spacing is smaller than the fitted one by a difference of *d*.

S.e Physical meaning of σ_N

From the size distribution analysis by TEM, we are aware that the synthesis produces nanocrystals of $CsPbBr_3$ with a distribution of edge lengths on the order of roughly ±1 nm (≈ ±2 unit cells),[3] which is correctly recovered by the Multilayer Diffraction method ($\sigma_N = 1.55$ unit cells). Directly transferring this size distribution onto Λ would make it incompatible with the superlattice interference, because the periodicity fluctuation must be on the order of a few Å to observe the superlattice fringes (see Equation 1 derived in section S.k). However, as demonstrated by Sevenhans *et. al.* on epitaxial multilayers, the superlattice diffraction can withstand larger fluctuations if they are distributed over multiples of the atomic lattice periodicity.[4] This is a sensible explanation for epitaxially grown multilayers, where the atomic planes are extended over dimensions much larger than the atomic plane thickness, and a fluctuation in the number of unit cells affects homogeneously the entire layer. In the case of nanocrystal superlattices, a fluctuation of the nanoparticle size would instead affect just a stacked column of particles. We argue that this would unavoidably destroy the superlattice structural coherence we observe, especially if repeated over the large number of layers found in each superlattice (~100 layers for a 1µm thick SL). As the coherence is observed in our experiments, we conclude that the self-assembly process is size-selective and individual superlattices (or superlattice regions) contain nanocrystals of the same size and shape. The size-selective nature of the self-assembly is a plausible explanation, as it has been previously reported in other systems.[5,6]

S.f Physical meaning of C

The superlattice interference effect requires several neighboring nanocrystals within the superlattice to be illuminated by a coherent radiation. This means that the phase of the incoming X-rays must be constant over a spatial region which contains multiple nanocrystals (coherence volume), so that only the phase mismatch due to the superlattice stacking periodicity produces interference. Despite being considered incoherent if compared with sources such as synchrotrons and free electron lasers, laboratory-grade X-ray diffractometers produce a beam which is coherent within a small volume. The degree of coherence depends on the instrumental configuration and on the incidence angle of the beam on the sample.

In principle, the factor *C* in Equations S9 should describe the number of nanocrystals which diffract coherently, *i.e.* the number of nanocrystals fitting into the coherence length of the X-ray beam. However, assessing the coherence length of the beam is useful only if another degree of coherence, the structural one, is high enough to make the difference appreciable. The stacking disorder of nanocrystals limits the effects of the beam coherence: above a certain threshold, increasing *C* does not produce any difference in the simulated pattern.

To investigate the influence of beam coherence on our experiments, we measured the same superlattice sample multiple times while gradually increasing the incident and receiving slits width in our diffractometer from 0.1 to 3 mm (Figure S5). The transversal component of the beam coherence, which is the one affecting the measurement the most, depends on the width of the source *D* (= slit width) and on the radius of the diffractometer *R*, which is constant.[7]

$$T_1 = \frac{\lambda R}{D} \qquad \text{Eq. 14}$$

A loss in the beam coherence should cause the superlattice diffraction pattern to resemble the diffraction profile of an individual nanocrystal. However, as Figure S5 shows, we found no effect attributable to a loss of coherence. The overall diffraction profile broadens due to the broader instrumental response function (Gaussian convolution). However, the peak asymmetry due to superlattice fringes is still visible with a 3 mm slit (≈ 24 nm coherence length, according to Equation S14, meaning only 2 nanocrystals diffracting coherently).

Our conclusion is that Equation S14 is inadequate to describe the coherence length in our beam. A likely reason is that Equation S14 is derived for a small spherical source, while our instrument uses a parallel beam geometry. Consequently, the resulting wave front is much flatter and therefore much more coherent than that expected for an isotropic source having the size of our slit. Consequently, the coherence length of our beam is large enough to be neglected, since the structural coherence of the superlattice lattice itself is low enough to dominate over the interference effect. For this reason, we picked a *C* value large enough that its variation has no impact on the fit result. We estimated that *C* = 20 is adequate for the purpose based on the χ^2 maps (see section S.h).

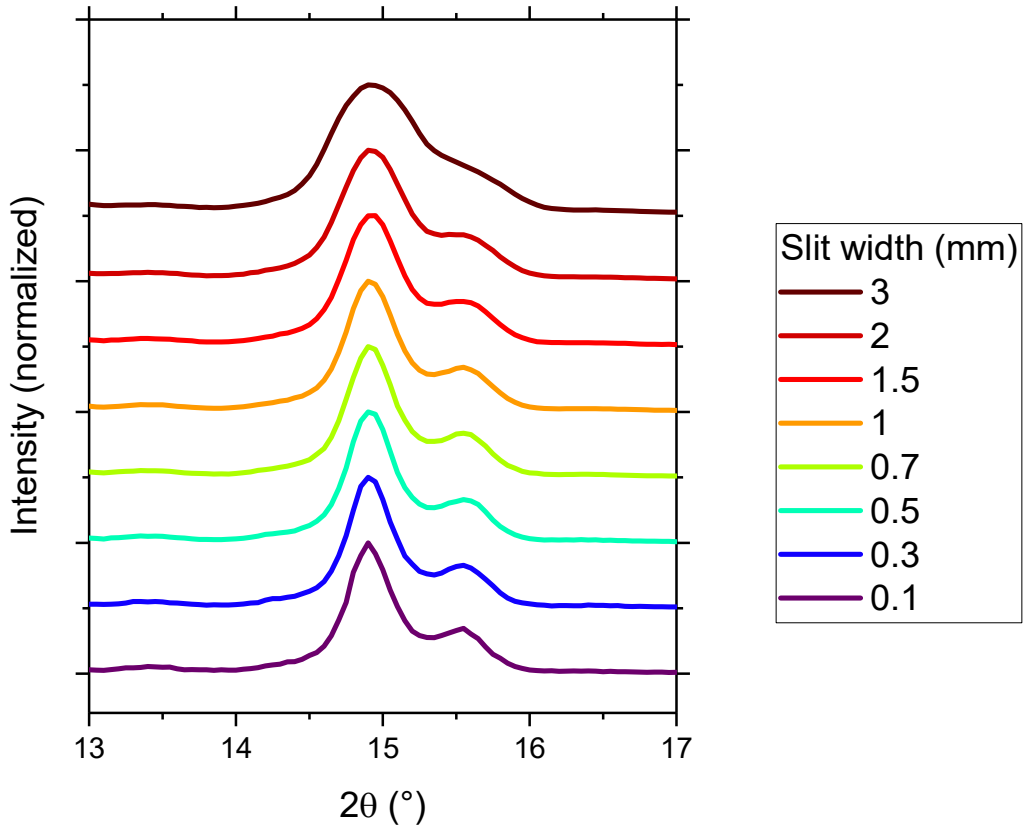

Figure S5. Effect of the slit width on the superlattice interference pattern. Increasing the diffractometer slit width increases the instrumental broadening (as seen by the smoothing of the diffraction profile) but does not cause the loss of the superlattice fringes (the Bragg peak profile remains structured), thus it is not altering the beam coherence length appreciably.

S.g Meaning of q-zero correction and fitting strategies

The q-zero correction represents a constant shift of the q-scale, which is meant to correct small misalignments of the diffractometer. It is based on the knowledge that some signals in a diffraction pattern, *e.g.* Bragg peaks of multiple diffraction orders and superlattice fringes, must be periodic in the q-scale. The q-zero correction shifts the scale so that this condition is exactly verified. To do so, the algorithm needs to include in the fit at least two signals belonging to the same periodicity: without this contribution the q-zero correction cannot be resolved from *d* and must be set to 0 $Å^{-1}$. This is the case of a single unstructured Bragg peak like that of PbS nanocrystal superlattices (Figure 6e),

If multiple fringes are visible, they can be exploited to perform the correction taking advantage of the multi-region fit option in our algorithm. For example, in the case of $CsPbBr_3$ and PbS nanoplatelets we fitted one extra fringe, chosen between q=0 $Å^{-1}$ and the analyzed Bragg peak. Its fit weight was set to 1/10 to minimize its influence on the other structural parameters: since *d* and the q-zero correction are underdetermined even a small contribution external to the Bragg peak is enough to resolve them. A similar strategy was applied for $CsPbBr_3$ nanocrystal superlattices. No extra fringes were available; thus, we exploited the periodicity of Bragg peaks by including the second one at a 1/10 weight. In principle both peaks could have been fitted with equal weight. However, the first Bragg peak is more informative of the superlattice structure: it is strongly modulated by the superlattice interference and is less affected by the $k\alpha_1/k\alpha_2$ polychromaticity of the beam and the orthorhombic peak splitting of the pseudocubic perovskite structure. These two effects combined cause a q-dependent peak broadening, which is stronger for the second Bragg peak: including it with equal weight would lead to an underestimation of the nanocrystal size.

S.h Parameter sensitivity and χ^2 maps for $CsPbBr_3$ nanocrystal superlattices

The Multilayer Diffraction algorithm includes the χ^2 maps as a tool to test the impact of parameters on the fit (Figure S6). Those plots show how the gradual variation of one single parameter affects the χ^2 of the fit (plotted on a logarithmic scale) while all the other parameters are kept constant. Most parameters feature a single and narrow minimum, indicating that the best fit parameter is uniquely determined, and the uncertainty is small (d, σ_L, S and q-zero correction). The parameter σ_N weakly affects the fit, hence it has a shallow minimum and is affected by a higher uncertainty. We set C = 20 in all our fits, as explained in the section S.f above.

The most peculiar behavior is that of L, which shows several minima separated by a period d from one another. That periodicity arises from the definition of Λ that interconnects L, N, and d, as defined in Equation S13 above. For a given sample, an integer change of N automatically involves a change of L by a multiple of d to keep Λ constant.

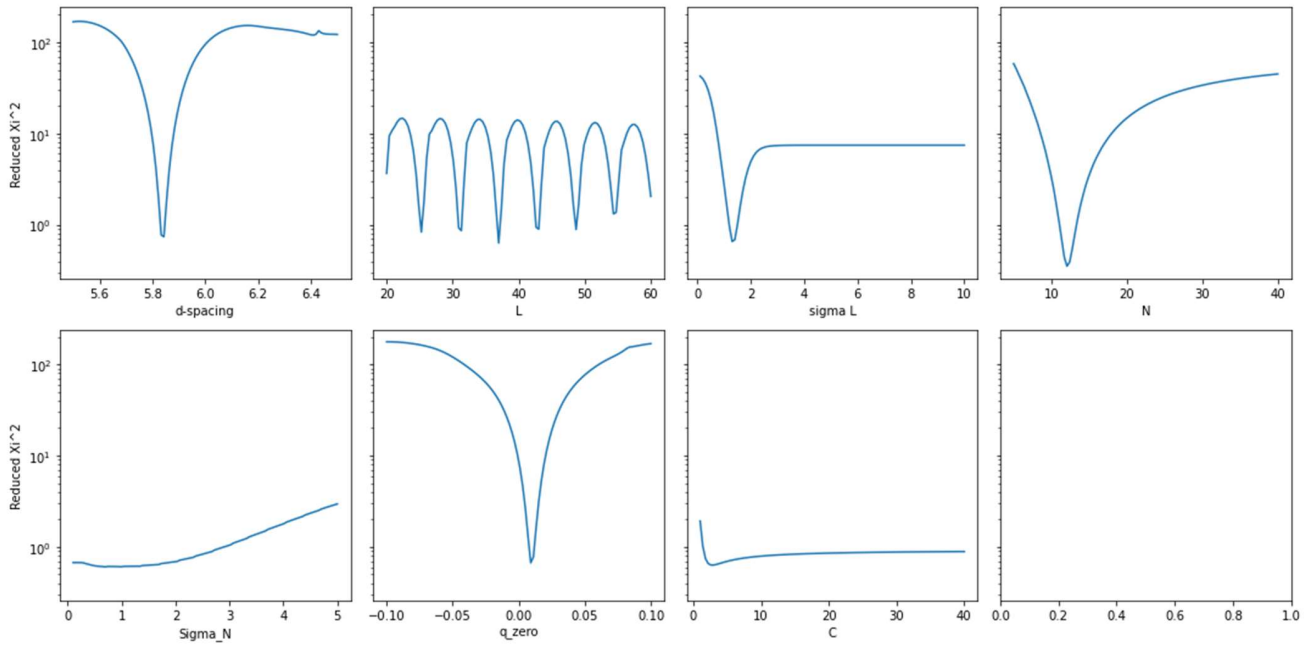

Figure S6. χ^2 maps, showing the effect of varying different parameters on the goodness of fit. The χ^2 maps shown here are from the fit of the room temperature $CsPbBr_3$ nanocrystal superlattice diffractogram.

S.i Experimental intensity fluctuation

The experimental intensity fluctuation was estimated by performing 3 repeated measurements on a room temperature $CsPbBr_3$ nanocrystal superlattice sample. For each measurement, the data was split into regions (low angle, 1st Bragg Peak, 2nd Bragg Peak) and normalized to produce data that is equivalent to what would be passed into the fit function. The average and standard deviation of relative intensity was calculated at each q-value. Errors on the intensity did not vary particularly strongly with relative intensity value, and were usually below 3% of the maximum value (see Figure S7). We used a flat error of 0.03 of the relative intensity values for most samples. Reduced χ^2 values at best fit (see Figure S6) with this assumed error are approximately 1, lending additional credence to this error estimation and fit quality.

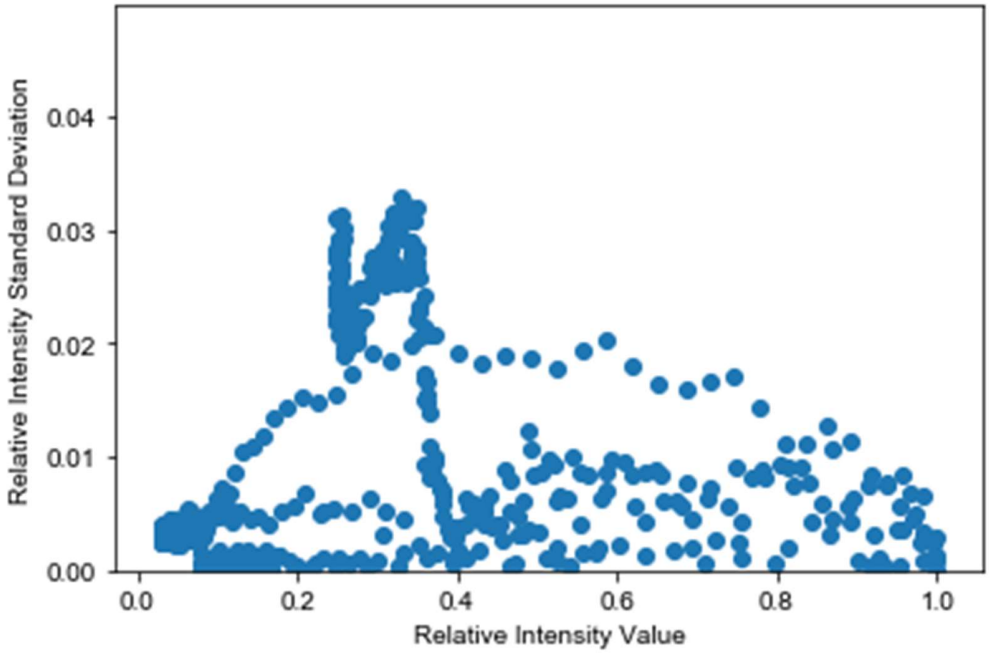

Figure S7. Scatter plot of standard deviation at different relative intensity values, measured on a replica sample of $CsPbBr_3$ nanocrystal superlattices.

S.j Bootstrap algorithm and correlation maps

Based on the error estimate in the preceding section, we used a bootstrap scheme to evaluate the uncertainty in the fit parameters. We assume an uncorrelated gaussian error between 2-5 % of the maximum value (depending on the sample). In the bootstrap algorithm, this error is incorporated into the fit by making modified simulated measurements with intensity values randomly selected from a gaussian distribution centered on the measured intensity value with a standard deviation defined by the gaussian error. This simulated measurement is then fit, and the parameter values are extracted. The average and standard deviation of these parameters over 100 repeated samples is reported in the main text.

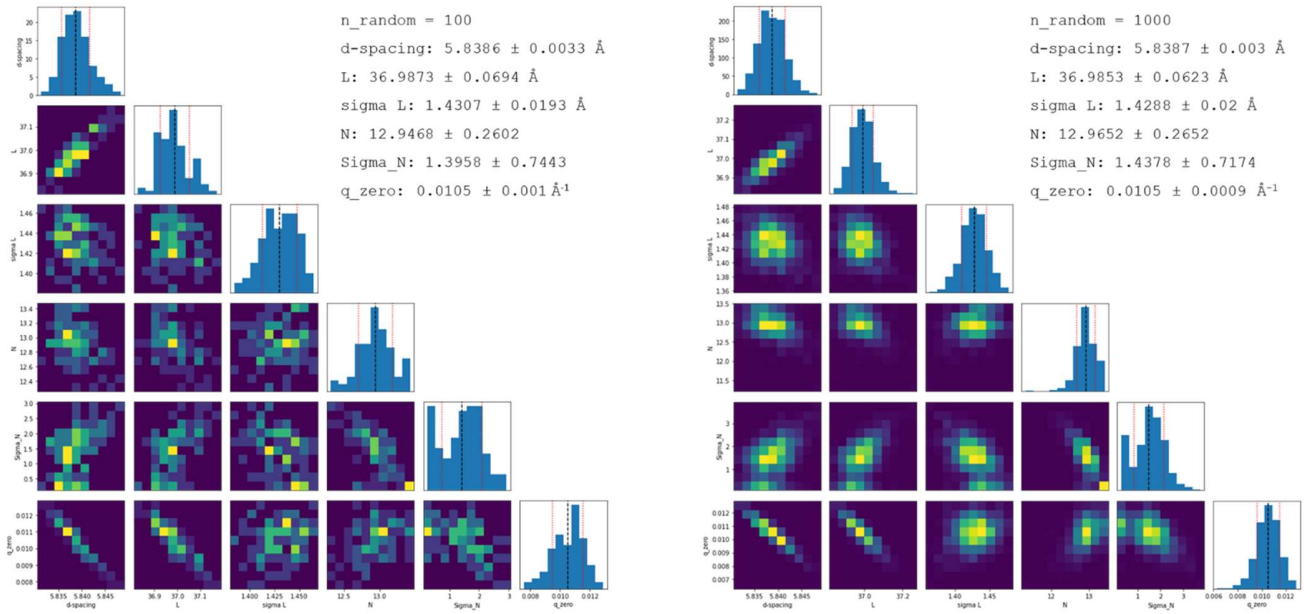

Figure S8. Bootstrap Histograms, in one dimension (diagonal elements) and two dimensions (off-diagonal elements), showing distribution and correlation of parameters from simulated measurements, together with the resulting averages and standard deviations of fitted parameters. The histograms are produced by using n = 100 iterations (left) and n=1000 iterations (right): the number of iterations can be increased (at the expense of increased computational time) by changing the value of “n_random ” parameter in the Deconvolution.py function file. The analyzed sample is $CsPbBr_3$ nanocrystal superlattices at room temperature (experimental data and script are anneal_RT.csv and anneal_RT.ipynb files, respectively).

S.k Derivation and application of Equation 1

The superlattice periodicity fluctuation can be estimated by finding the misplacement needed to make X-rays scattered by one nanocrystal interfere destructively with X-rays scattered by its perfectly stacked neighbors. For a perfect superlattice with a periodicity Λ_0, X-rays interfere constructively at an angle θ_0 determined by Bragg's law:

$$n\lambda = 2\Lambda_0 \sin(\theta_0) \qquad \text{Eq. S15}$$

We now consider a nanocrystal stacked at an imperfect distance $\Lambda = \Lambda_0 \pm \delta_\Lambda$, where δ_Λ represents its misplacement. The interference observed at the original angle θ_0 will become less and less constructive the more δ_Λ increases. The δ_Λ at which the interference becomes completely destructive is found by imposing n ± ½ instead of *n* on the left side in Bragg's law:

$$\left(n \pm \tfrac{1}{2}\right)\lambda = 2\Lambda \sin(\theta_0) \qquad \text{Eq. S16}$$

Substituting Equation S16 for $\sin(\theta_0)$ gives:

$$\left(n \pm \tfrac{1}{2}\right)\lambda = 2\Lambda \cdot \frac{n\lambda}{2\Lambda_0} \qquad \text{Eq. S17}$$

$$n\Lambda_0 \pm \tfrac{1}{2}\Lambda_0 = n\Lambda \qquad \text{Eq. S18}$$

Substituting $\Lambda = \Lambda_0 \pm \delta_\Lambda$ produces:

$$n\Lambda_0 \pm \tfrac{1}{2}\Lambda_0 = n\Lambda_0 \pm n\delta_\Lambda \qquad \text{Eq. S19}$$

$$\delta_\Lambda = \pm\frac{\Lambda_0}{2n} \qquad \text{Eq. S20}$$

Equation S20 indicates the misplacement needed to bring a nanocrystal into completely destructive interference conditions with the rest of the SL. However, we are more interested in the loss of constructive interference, which occurs when totally constructive and totally destructive interference have the same probability. Thinking of δ_Λ as an average misplacement, this occurs when δ_Λ is equal to half the value found by Equation S20. Finally, this implies that if we can see the superlattice effect decorating a Bragg peak, the average displacement must be smaller than this threshold:

$$\delta_\Lambda \leq \frac{\Lambda_0}{4n} = \frac{\pi}{2q} \qquad \text{Eq. S21 = Eq. 1}$$

Where $n = \frac{q\Lambda_0}{2\pi}$ represents the index of the superlattice fringe (like that of a Bragg peak). Equation 1 can be used as a figure of merit to estimate the superlattice stacking disorder by the inspection of the Bragg peaks fine structure, with no need of a full profile fit. An example of application on $CsPbBr_3$ nanocrystal superlattices follows. First, inspect the diffractogram (Figure 1c, main text) and notice that the first Bragg peak (q = 1.1 $Å^{-1}$) shows superlattice fringes while the second (q = 2.2 $Å^{-1}$) does not. Then, calculate δ_Λ at both peaks using Equation 1, finding that δ_Λ ≈ 1.4 Å for the first and δ_Λ ≈ 0.7 Å for the second. The first Bragg peak shows superlattice fringes, therefore the average displacement must be smaller than the calculated value. On the contrary, the second Bragg peak is not modulated by the superlattice interference, and the structural disorder must be higher than the related threshold. Thus, we shall conclude that 0.7 Å < δ_Λ < 1.4 Å. Note that $\delta_\Lambda \neq \sigma_\Lambda$: the first is an average misplacement, while the second is the standard deviation of a Gaussian distribution. However, the two parameters share the same order of magnitude.

S.I Comparison with GISAXS, GIWAXS and SAED

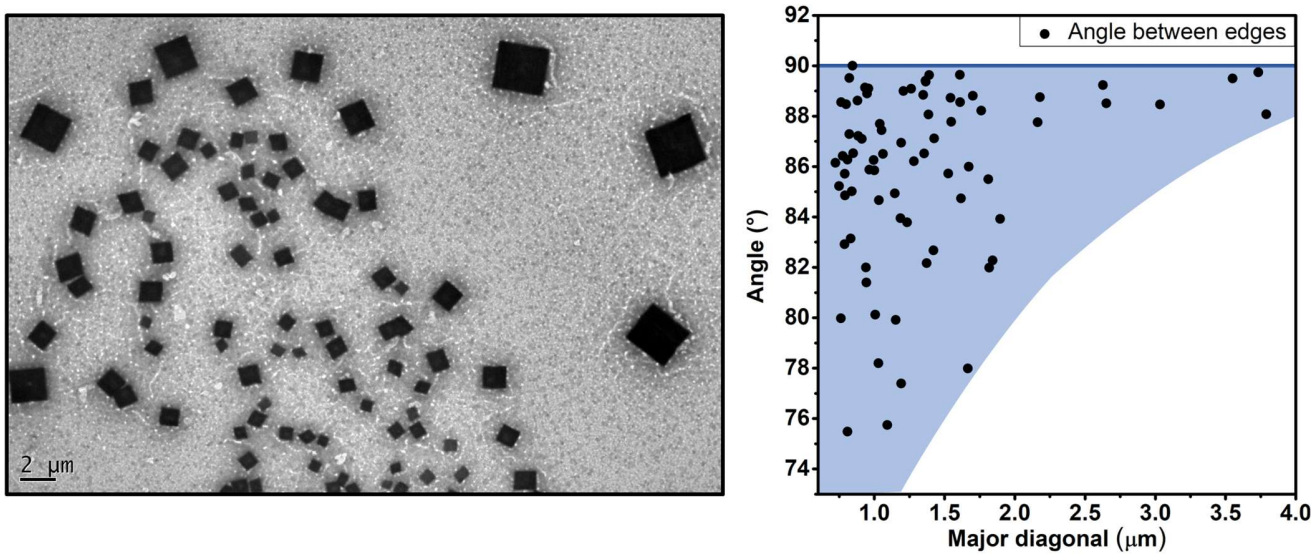

Figure S9. The role of size on the structure of $CsPbBr_3$ nanocrystal superlattices. a) TEM image of several $CsPbBr_3$ superlattices grown on the same mesh. b) Plot relating the size of each superlattice (indicated by its major diagonal) to its distortion from a perfect square/rectangle.

Figure 3b shows a GISAXS pattern collected from a film of $CsPbBr_3$ nanocrystal superlattices. Signal comes in form of spots, demonstrating that nanocrystals are periodically stacked along all the three spatial directions as expected for a 3D-superlattice. Given the thickness of our superlattices (up to 1 μm ≈ 100 layers), this suggests that underlying nanocrystal templated the growth of those on the top, avoiding superlattice plane shifts or rotations. The shape of the spots, narrow and well defined, attests the high structural order of superlattices. However, quantifying the degree of order by GISAXS would entail measuring the bidimensional instrumental broadening and deconvoluting its contribution over a bidimensional map, that is a challenging task. GISAXS spots were indexed with the SUNBIM software,[8] and are compatible with a primitive cubic packing of nanocrystals. The extracted horizontal and vertical periodicities of 103.9 ± 0.4 Å and 103.0 ± 1.1 Å suggest that packing is isotropic within the instrumental resolution (Figure 1b).

Figure 3c-d shows a side-by-side comparison of GIWAXS and SAED. The $CsPbBr_3$ nanocrystals used in this work have an orthorhombic structure, however the differences from the ideal cubic structure are small and dynamic.[9–12] Thus, both patterns were indexed according to a pseudo-cubic description for simplicity. Despite showing similarities, GIWAXS and SAED patterns are different: with respect to our sample GIWAXS is a powder-like ensemble measurement that includes signals coming from all the nanocrystal atomic planes, while SAED is a single-superlattice measurement sensitive only to the planes perpendicular to the substrate. The GIWAXS pattern contains well-defined spots, slightly elliptical in the annular direction. As for GISAXS, this suggests a high structural order, which is again challenging to quantify. In addition, they attest to the extremely selective orientation of individual nanocrystals in the sample (laying with the pseudocubic {100} planes parallel to the substrate). The arc at ~0.9 $Å^{-1}$ comes from an unidentified impurity, perhaps the same found in the θ:2θ XRD pattern (Figure 1c). However, the arc shape implies that, whatever structure is formed, it must be randomly oriented, which rules out any contribution from the nanocrystals.

In both GIWAXS and SAED, the annular broadening of spots arises from the tilt of the individual nanocrystals with respect to the X-ray/electron beam axis.[13] This is more pronounced in the SAED pattern, while in the GIWAXS it is minimal. The difference is mainly due to smaller superlattices (measured by SAED) being more distorted than larger ones. In fact, the inspection of several superlattices in TEM revealed that smaller superlattices have a higher chance of being distorted from the ideal squared/rectangular shape, which we can take as an indicator of structural perfection (Figure S9). This explains why superlattices studied in SAED, for which thin (and therefore small) superlattices are needed, are more prone to nanocrystal tilting. In addition, the horizontal direction of growth probed in SAED does not benefit from the substrate templating effect, whereas the vertical direction probed in GIWAXS does. This might lead to the structural disorder in the horizontal direction being slightly higher, even if we argue that this effect is probably negligible. In fact, no trace of visible mosaicity was in found in HRSEM images of superlattices grown on silicon substrates (Figure 1b).

To summarize and compare with the Multilayer Diffraction model, the picture provided by GISAXS, GIWAXS and SAED is that $CsPbBr_3$ nanocrystals superlattices feature a primitive cubic packing that is ordered and periodic in all the three spatial directions. This information cannot be extracted from the Multilayer Diffraction method, which is inherently monodimensional. Nanocrystals inside the superlattice are oriented with the pseudocubic {h00} planes parallel to the substrate. Since nanocrystals are orthorhombic, this could be in principle distinguished as one of two non-equivalent orientations (pseudocubic {h00} = (020)+{101} orthorhombic) or a random mixture of them, but the resolution of GIWAXS/SAED is insufficient for this purpose. The narrow spots in GISAXS and GIWAXS indicate a high structural order all over the sample. However, extracting quantitative information about the disorder is challenging, while it is readily available by the Multilayer Diffraction model, although limited to the vertical direction. The same goes for parameters such as nanocrystal size, interparticle spacing and their distributions, which would require a complex fit of the GISAXS/GIWAXS scattering maps and are instead easily recovered by the Multilayer Diffraction method.

S.m Thermal annealing of $CsPbBr_3$ nanocrystal superlattices

Figure S10 shows the evolution of the most important features in the $CsPbBr_3$ nanocrystal superlattices pattern upon thermal annealing. All the patterns evolve in the 25-150°C temperature range. The evolution of the first Bragg peak profile is commented in the main text, with reference to Figure 4. In addition, the overall intensity of the peak increases due to a better alignment of nanocrystals with the substrate surface, compatibly with an improvement of the superlattice structural order. The same effect is found for the superlattice Bragg peak at low angles ($2\theta \approx 1.75°$) and the second Bragg peak ($2\theta \approx 30.5°$). Interestingly, panel c) demonstrates that the second Bragg peak is not completely unaffected by the superlattice effect, as the gradually increasing structural order of the superlattice is captured by the appearance of a weak peak profile modulation.

At 150°C a sudden drop of the diffracted intensities occurs in all regions, together with the loss of superlattice fringes and the sharpening of the Bragg peak profile. This is compatible with the sudden sintering of nanocrystals within the superlattice structure, that introduces disorder (loss of superlattice fringes, loss of superlattice Bragg peak), misaligns the atomic planes (decrease in the diffracted intensity) and causes the formation of larger crystallites (sharper Bragg peak profiles).

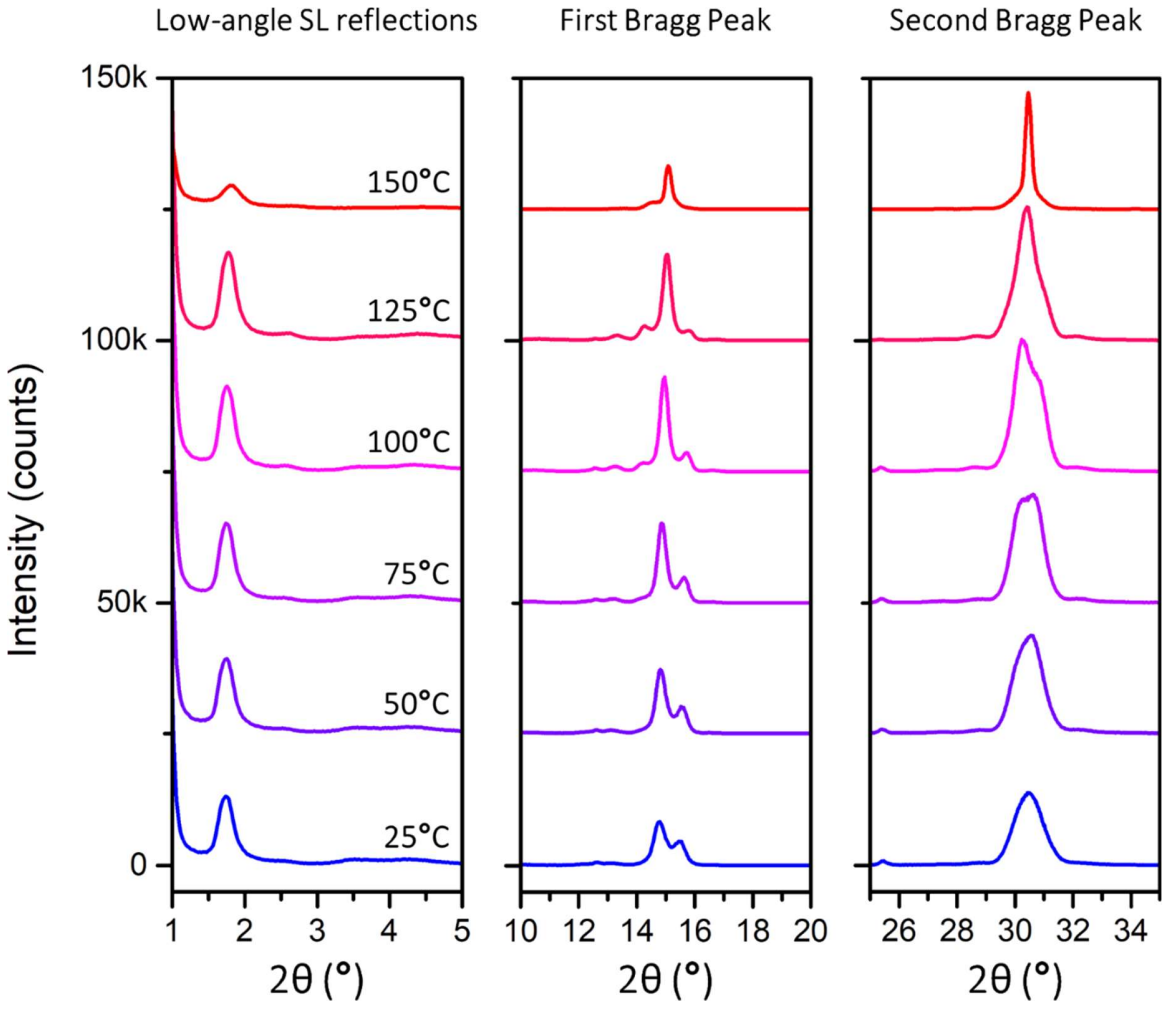

Figure S10. Thermal annealing of $CsPbBr_3$ nanocrystal superlattices. Evolution of all the regions in the $CsPbBr_3$ nanocrystal superlattices pattern upon thermal annealing. Intensities are not normalized.

S.n N and σ_N evolution during thermal annealing

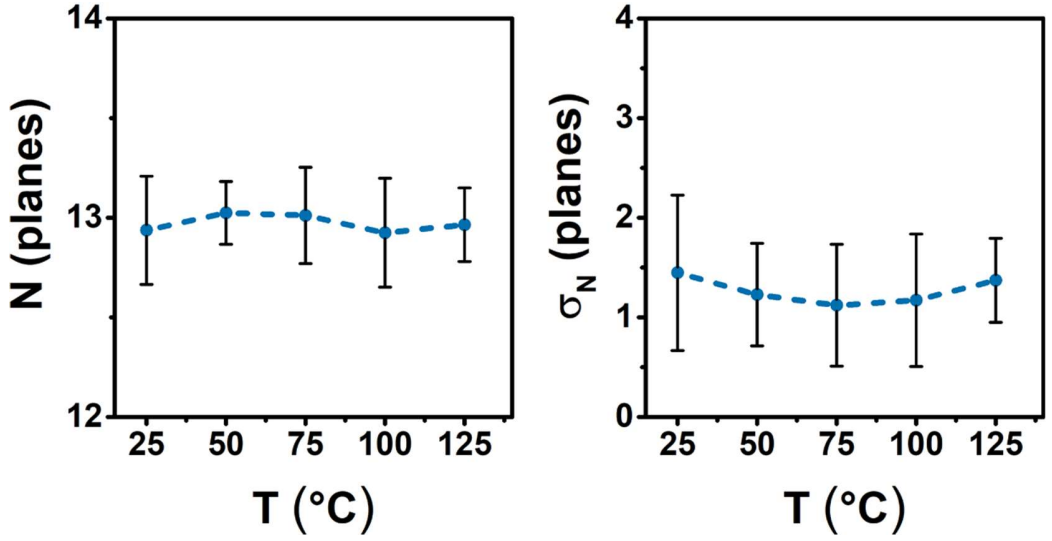

Figure S11. N and σ_N evolution during thermal annealing. As expected in the absence of nanocrystals coalescence, the nanocrystal size *S* and size distribution σ_N remained constant in the 25-125°C range, with fluctuations within the error bars.

S.o $CsPbBr_3$ nanoplatelets data treatment and anisotropic lattice expansion

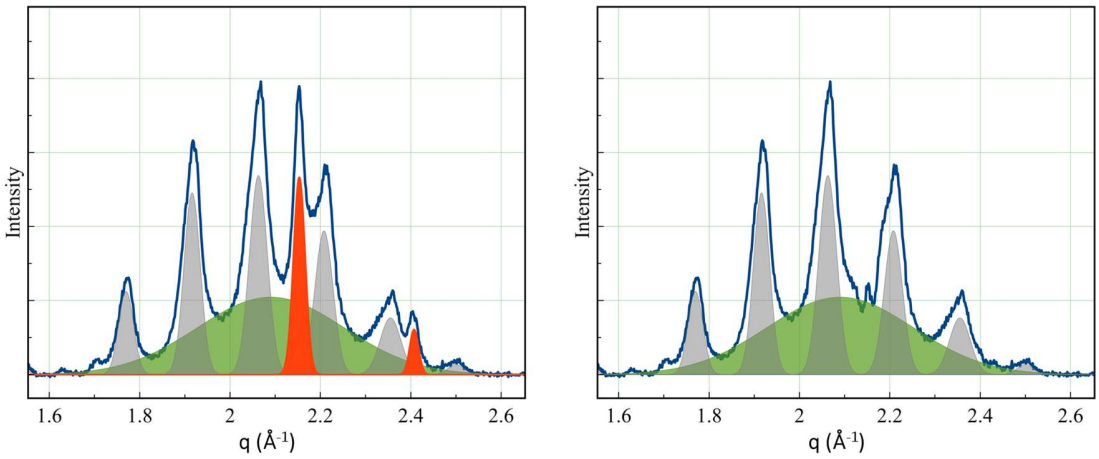

Figure S12. Preparing $CsPbBr_3$ nanoplatelets pattern for the fit. The as-acquired pattern (left) was fitted with a series of gaussian curves, representing the diffuse scattering (green), the superlattice fringes (grey) and two spurious peaks (red) not belonging to the superlattice interference pattern. Those were subtracted to obtain the pattern fitted by the Multilayer Diffraction method (right).

The as-acquired diffraction pattern of $CsPbBr_3$ nanoplatelets contains two peaks which are not compatible with superlattice fringes: they are sharper than the peaks surrounding them, and their position in the q.-scale does not follow the periodicity of superlattice fringes. These outlier peaks are identified as the (220)/(004) peak (q=2.15 $Å^{-1}$) and (114)/(222) peak of $CsPbBr_3$, visible due to the non-oriented nanoplatelets present in the sample. The outlier peaks were fitted with a Gaussian peak shape and subtracted before performing the multilayer diffraction fit.

However, the presence of the (220)/(004) peak is useful to study the anisotropic lattice expansion found in $CsPbBr_3$ nanoplatelets. Its position is compatible with a pseudocubic d = 5.836 Å, compatible with that of cuboidal nanocrystals. The peak shape is sharp, indicating that the reflection comes from the spatially-extended direction of the nanoplatelets. The superlattice interference convolution profile, instead, is clearly shifted towards lower angles, compatibly with d = 6.0166 Å resulting from the fit. This clearly indicates that $CsPbBr_3$ nanoplatelets undergo an anisotropic lattice expansion along their thinner direction (+3.0%).

S.p PbS nanocrystal superlattices χ^2 maps and rotational disorder

The χ^2 maps for PbS nanocrystal superlattices (Figure S13) show that σ_L produces the best fit for any value above ≈ 1.5 Å. This clearly indicates that the superlattice interference is completely absent for this sample. As consequently expected, *L* plays no role in the fit, because the pattern contains no information at all about the relative arrangement of nanocrystals within the SL. It is worth noting that σ_L represents a linear misplacement, but for spheroidal nanoparticles some tilting disorder is to be expected as well. This, however, can be expressed as a linear displacement *via* a simple geometrical relation:

$$\alpha = \arctan\left(\frac{2\sigma_L}{W}\right) \qquad \text{Eq. S22}$$

Where $W = (N-1)\cdot d$ is the width of the nanocrystal expressed in Å. Applying Equation 22 to the estimated σ_L > 1.5 Å yields a titling misplacement of α > 1.9°, which is enough to destroy the superlattice interference while still maintaining a high preferred orientation for nanocrystals. The physical reality combines both a linear and an angular tilting, of which σ_L represents a collective measurement.

Interestingly, σ_S is unusually high for such a highly monodisperse sample (as seen by TEM, Figure 6g). This is probably due to the spherical shape of nanocrystals, that causes the nanocrystal vertical thickness to change between center and borders, and might even cause a slight underestimation of the nanocrystal size *S*.

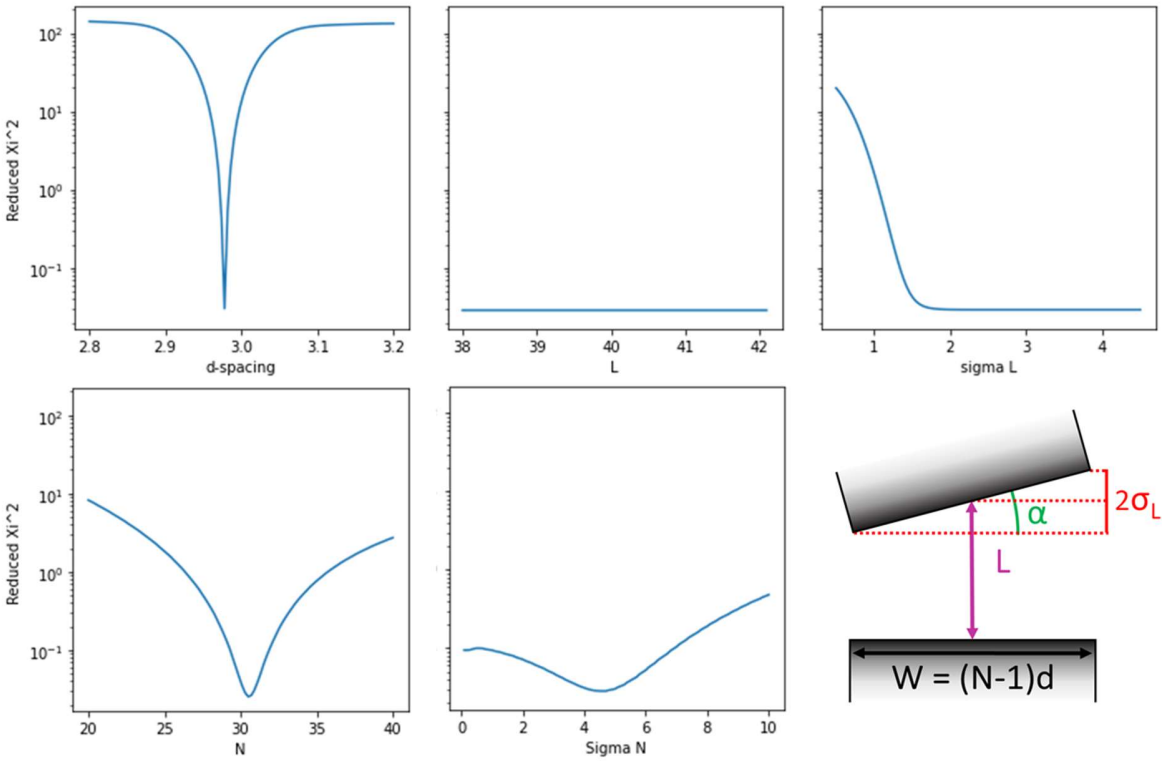

Figure S13. χ^2 maps for PbS nanocrystal superlattices, together with a scheme explaining the effect of nanocrystal tilting on the misplacement parameter σ_L.

S.q Effects of the Lorentz-Polarization correction

The Lorentz-Polarization correction is a procedure applied to the as-measured diffractograms to compensate for two angle-dependent alterations of the diffracted intensity. Specifically, the polarization correction takes into account the contribution of the polarization of the incident beam, while the Lorentz correction accounts for the different time crystallites remain within diffraction conditions at different measurement angles.

The q-scale diffraction data fitted in this work was obtained from the experimentally measured $I(2\theta)$ by dividing it with the Lorentz-polarization factor, $Lp = \frac{(1+A\cos^2 2\theta)}{(1+A)\sin 2\theta}$, where $A = cos^2 2\theta_M$ and θ_M is the Bragg angle of the monochromator crystal (1° in our case).[14]

Figure S14 compares the diffractogram and fit results of PbS nanosheets before and after the application of the Lorentz-Polarization correction. This example was chosen because the Lorentz-Polarization correction mostly affects the relative intensities of signals which are far from each other in the q-scale.

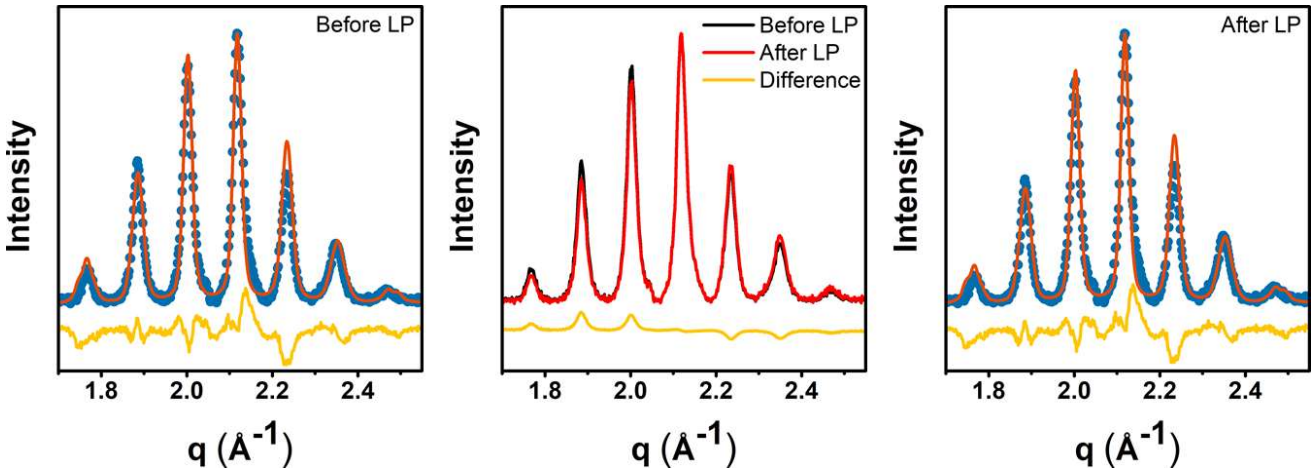

Figure S14. PbS nanosheets patterns and fits before and after the application of the Lorentz-polarization correction.

Table 1. Fit results for PbS nanoplatelet assemblies before and after the Lorentz-polarization correction.

Sample	*d* (Å)	*L* (Å)	σ_L (Å)	*N* (planes)	σ_N (planes)	Λ (Å)
Before LP Correction	3.0233 ± 0.0042	44.3933 ± 0.029	0.324 ± 0.016	3.98 ≈ 4 ± 0.05 (9.07 Å thick)	0.817 ± 0.078	53.463 ± 0.032
After LP Correction	3.0083 ± 0.0042	44.444 ± 0.024	0.325 ± 0.017	3.98 ≈ 4 ± 0.05 (9.07 Å thick)	0.850 ± 0.080	53.469 ± 0.027

S.r List of provided files

- Microsoft Excel Spreadsheet for XRD data conversion from 2θ(°)/Intensity format to q(Å^{-1})/Lp-corrected Intensity format: *Data Conversion.xlsx*

- Python function file required for running the Jupyter Notebooks, that contains the multilayer diffraction fitting algorithm: *Deconvolution.py*

- XRD datafiles [q(Å^{-1})/Lp-corrected Intensity]:
    - Of $CsPbBr_3$ nanocrystal superlattices at different temperatures: *anneal_RT: anneal_50; anneal_75; anneal_100; anneal_125 (.csv)*
    - Of $CsPbBr_3$ nanoplatelet stacks: *CsPbBr3_nanoplatelets.csv*
    - Of PbS nanoplatelet stacks: *PbS_nanoplatelets.csv*
    - Of PbS nanocrystal superlattices: *PbS_nanocrystals.csv*

- Jupyter Notebooks file with fitting routine and bootstrapping error analysis:
    - Of $CsPbBr_3$ nanocrystal superlattices at different temperatures: *anneal_RT: anneal_50; anneal_75; anneal_100; anneal_125 (.ipynb)*
    - Of $CsPbBr_3$ nanoplatelet stacks: *CsPbBr3_nanoplatelets.ipynb*
    - Of PbS nanoplatelet stacks: *PbS_nanoplatelets.ipynb*
    - Of PbS nanocrystal superlattices: *PbS_nanocrystals.ipynb*

- Output of the Jupyter Notebooks fitting routines in the format of a multicolumn data file:
    - Of $CsPbBr_3$ nanocrystal superlattices at different temperatures: *FIT_anneal_RT: FIT_anneal_50; FIT_anneal_75; FIT_anneal_100; FIT_anneal_125 (.csv)*
    - Of $CsPbBr_3$ nanoplatelet stacks: *FIT_CsPbBr3_nanoplatelets.csv*
    - Of PbS nanoplatelet stacks: *FIT_PbS_nanoplatelets.csv*
    - Of PbS nanocrystal superlattices: *FIT_PbS_nanocrystals.csv*

S.s References

(1) Fullerton, E. E.; Schuller, I. K.; Vanderstraeten, H.; Bruynseraede, Y. Structural Refinement of Superlattices from X-Ray Diffraction. *Phys. Rev. B* **1992**, *45*, 9292–9310.

(2) Toso, S.; Baranov, D.; Giannini, C.; Marras, S.; Manna, L. Wide-Angle X-Ray Diffraction Evidence of Structural Coherence in $CsPbBr_3$ Nanocrystal Superlattices. *ACS Mater. Lett.* **2019**, *1*, 272–276.

(3) Baranov, D.; Toso, S.; Imran, M.; Manna, L. Investigation into the Photoluminescence Red Shift in Cesium Lead Bromide Nanocrystal Superlattices. *J. Phys. Chem. Lett.* **2019**, *10*, 655–660.

(4) Sevenhans, W.; Gijs, M.; Bruynseraede, Y.; Homma, H.; Schuller, I. K. Cumulative Disorder and X-Ray Line Broadening in Multilayers. *Phys. Rev. B* **1986**, *34*, 5955–5958.

(5) Lin, Y.; Skaff, H.; Emrick, T.; Dinsmore, A. D.; Russell, T. P. Nanoparticle Assembly and Transport at Liquid-Liquid Interfaces. *Science.* **2003**, *299*, 226–229.

(6) Schöpe, H. J.; Bryant, G.; Van Megen, W. Effect of Polydispersity on the Crystallization Kinetics of Suspensions of Colloidal Hard Spheres When Approaching the Glass Transition. *J. Chem. Phys.* **2007**, *127*, 084505.

(7) Xiong, G.; Moutanabbir, O.; Reiche, M.; Harder, R.; Robinson, I. Coherent X-Ray Diffraction Imaging and Characterization of Strain in Silicon-on-Insulator Nanostructures. *Adv. Mater.* **2014**, *26*, 7747–7763.

(8) Siliqi, D.; De Caro, L.; Ladisa, M.; Scattarella, F.; Mazzone, A.; Altamura, D.; Sibillano, T.; Giannini, C. SUNBIM: A Package for X-Ray Imaging of Nano- and Biomaterials Using SAXS, WAXS, GISAXS and GIWAXS Techniques. *J. Appl. Crystallogr.* **2016**, *49*, 1107–1114.

(9) Bertolotti, F.; Protesescu, L.; Kovalenko, M. V.; Yakunin, S.; Cervellino, A.; Billinge, S. J. L.; Terban, M. W.; Pedersen, J. S.; Masciocchi, N.; Guagliardi, A. Coherent Nanotwins and Dynamic Disorder in Cesium Lead Halide Perovskite Nanocrystals. *ACS Nano* **2017**, *11*, 3819–3831.

(10) Cottingham, P.; Brutchey, R. L. On the Crystal Structure of Colloidally Prepared $CsPbBr_3$ Quantum Dots. *Chem. Commun.* **2016**, *52*, 5246–5249.

(11) Brennan, M. C.; Kuno, M.; Rouvimov, S. Crystal Structure of Individual $CsPbBr_3$ Perovskite Nanocubes. *Inorg. Chem.* **2019**, *58*, 1555–1560.

(12) Jung, Y. K.; Butler, K. T.; Walsh, A. Halide Perovskite Heteroepitaxy: Bond Formation and Carrier Confinement at the PbS-$CsPbBr_3$ Interface. *J. Phys. Chem. C* **2017**, *121*, 27351–27356.

(13) Van Der Burgt, J. S.; Geuchies, J. J.; Van Der Meer, B.; Vanrompay, H.; Zanaga, D.; Zhang, Y.; Albrecht, W.; Petukhov, A. V.; Filion, L.; Bals, S.; Swart, I.; Vanmaekelbergh, D. Cuboidal Supraparticles Self-Assembled from Cubic $CsPbBr_3$ Perovskite Nanocrystals. *J. Phys. Chem. C* **2018**, *122*, 15706–15712.

(14) Lorentz–polarization correction (Online Dictionary of Crystallography) https://dictionary.iucr.org/Lorentz–polarization_correction (accessed Dec 16, 2020).